Numerical validation and back-pressure effect on internal compression flows of typical supersonic inlet

F. Ding
dingcuifengdcf@163.com
C.-B. Shen
cbshen@nudt.edu.cn
W. Huang and J. Liu
College of Aerospace Science and Engineering
Science and Technology on Scramjet Laboratory
National University of Defense Technology
Hunan
China

ABSTRACT

A numerical study was conducted to analyse the performance of different turbulence models and different turbulence intensities and turbulence length scales specified for the boundary condition of the inflow to the internal compression flow field of a typical supersonic inlet. The effect of the back-pressure ratio on the properties of the flow field was also investigated. Computational results obtained by the commercial software FLUENT, which is used to solve the full two-dimensional Reynolds-averaged Navier-Stokes equations, were validated through both graphical and quantitative comparisons with previously published experimental data. The two-equation models that were considered in this study are the RNG k-ε, realisable k-ε, standard k-ε, and SST k-ω turbulence models. The RNG k-ε model had the best performance among the four models and predicted good wall pressure distributions. The best agreement between the predicted results and experimental data was obtained when either the default values of the freestream turbulence intensity and length scale in the FLUENT solver were used, or the empirical formula was used to calculate the two parameters of the freestream turbulence properties. The shock wave pattern varied between the oblique mode and the fully developed normal mode with increasing back-pressure ratio, and the unstart phenomenon occurred when the back-pressure ratio was sufficiently high.

Paper No. 4182. Manuscript received 8 May 2014, revised version received 30 November 2014, accepted 11 December 2014.

https://doi.org/10.1017/S0001924000010721 Published online by Cambridge University Press

NOMENCLATURE

V	validation metric
M_∞	free-stream Mach number
Re_∞	free-stream Reynolds number per unit, 1/m
P_0	free-stream total pressure, N/m^2
T_0	free-stream total temperature, K
P_∞	free-stream static pressure, N/m^2
P/P_0	ratio of local static pressure to free-stream total pressure
P_{back}/P_∞	back-pressure ratio = Ratio of back pressure to free-stream static pressure
I	turbulence intensity
l	turbulence length scale, m
D_H	hydraulic diameter of flow path, m
Re_{DH}	Reynolds number per unit based on D_H, 1/m

1.0 INTRODUCTION

Future hypersonic cruise vehicles will require highly integrated and efficient propulsion systems. The possibility of achieving this will depend significantly on progress made in computational fluid dynamics for high-speed flows. Hypersonic flows are characterised by high Mach numbers in the inviscid region, high gradients of the flow variables in the vicinity of shocks, real gas effects, and thick heated boundary layers[1]. Presently, a number of very powerful and efficient computational codes such as the commercial software ANSYS FLUENT[2] are available for solving the full Navier–Stokes equations. However, the efficiencies (convergence speed and accuracy) of these codes depend, among other factors, on the type of turbulence modeling they implement.

Two-equation turbulence models allow the determination of both a turbulent length and time scale by solving two separate transport equations[2]. The standard k-ε model which was proposed by Lauder and Spalding[3] is widely used in engineering computational models, where k is the turbulence kinetic energy per unit mass and ε is the rate of dissipation of k. Its robustness, economy, and reasonable accuracy for a wide range of turbulent flows make it popular in industrial flow and heat transfer simulations[2]. However, this model has several shortcomings that make it especially unsuitable for hypersonic flows. For example, the model is very inaccurate for even the mildest of adverse pressure gradients, and it is extremely difficult to integrate through a viscous sublayer[1]. As the strengths and weaknesses of the standard k-ε model have become known, modifications have been introduced to improve its performance. Two of these variants are available in ANSYS FLUENT[2], namely the RNG k-ε[4] and realisable k-ε models[5]. The RNG k-ε model is derived from the instantaneous Navier-Stokes equations, using a mathematical technique called 'renormalisation group' (RNG) methods, and it is more responsive to the effects of rapid strain and streamline curvature than the stand k-ε model, which explains the superior performance of the RNG model for certain classes of flows[4]. The realisable k-ε model differs from the standard k-ε model in two important ways. Firstly, the realisable k-ε model contains an alternative formulation for the turbulent viscosity. Secondly, a modified transport equation for the dissipation rate, ε, has been derived from an exact equation for the transport of the mean-square vorticity fluctuation[5]. Both the RNG and k-ε realisable models have shown substantial improvements over the standard k-ε model where the flow features include strong streamline curvature, vortices, and rotation[2].

The k-ω models form the second most widely used class of turbulence models. Two widely used k-ω models, which are also available in ANSYS FLUENT[2], are due to the standard k-ω

https://doi.org/10.1017/S0001924000010721 Published online by Cambridge University Press

and SST k-ω models[6]. The standard k-ω model in ANSYS FLUENT is based on the Wilcox k-ω model[7-9] which incorporates modifications for low-Reynolds-number effects, compressibility, and shear flow spreading. It is an empirical model based on model transport equations for the turbulence kinetic energy (k) and the specific dissipation rate (ω), which can also be thought of as the ratio of ε to k. The shear-stress transport (SST) k-ω model was developed by Menter[10-12] to effectively blend the robust and accurate formulation of the k-ω model in the near-wall region with the freestream independence of the k-ε model in the far field. Its particular features make the SST k-ω model more accurate and reliable for a wider class of flows than the standard k-ω model[2]. The SST model was originally used for aeronautics applications, but has made its way into most industrial, commercial and many research codes[11].

In evaluating turbulence models for the hypersonic inlet, Kapoor *et al*[13] studied the performance of various turbulence models when applied to the hypersonic NASA P8 inlet. The zero-equation models considered for this study were the Baldwin-Lomax model, the Thomas model, and a combination of the Baldwin-Lomax and Thomas models. The two-equation models considered were the Chien model, the Speziale model (both low Reynolds number), and the Launder and Spalding model (high Reynolds number). The Thomas model performed best among the zero-equation models, and predicted good pressure distributions. The Chien and Speziale models compared very well with the experimental data, and performed better than the Thomas model near the walls[13]. However, they did not utilise any validation metrics to estimate the discrepancy between the predicted results and the experimental data quantitatively.

In a numerical simulation, it is appropriate to specify a uniform value for the turbulence quantity at the inflow boundary, especially when the profiles of the turbulence quantities are not accurately known[2]. Turbulence intensity and turbulence length scale are two convenient parameters for specifying turbulence properties. The study of the effects of the different turbulence intensities and length scales specified in the inflow boundary condition of a supersonic inlet is essential for the improvement of numerical accuracy.

The typical validation procedure in CFD and other fields involves graphical comparison of computational results and experimental data. If the computational results 'generally agree' with the experimental data, the computational results would be declared 'validated.' A graphical comparison of computational results and experimental data is, however, only marginally better than a qualitative comparison. In a graphical comparison, quantification of the numerical error or computational uncertainties is not commonly apparent owing to the absence of the initial conditions, boundary conditions, or modeling parameters. A graphical comparison also offers little quantitative indication of the variation in the agreement over the range of the independent variable (e.g., space or time) or the parameter of interest (i.e., the Reynolds number or a geometric parameter). Quantifying the level of agreement between computational results and experimental data during the validation, which is referred to as a validation metric[14], is an important research topic. When the experimental measurement error is zero, one useful validation metric based on the comparison of the experimental measurement and the computational result at each measurement location is as follows[15]:

$$V = 1 - \frac{1}{N}\sum_{i=1}^{N} \mathrm{Tanh}\left|\frac{y(x_i) - Y(x_i)}{Y(x_i)}\right| \qquad \ldots (1)$$

Here, V is the validation metric and $Y(x_i)$ is the experimental measurement corresponding to the dependent variable y at $x = x_i$ for $i = 1,2,3, \ldots, N$. This metric has the following advantages. First, it normalises the differences between the computational results and experimental data. Second, the absolute value of the relative error permits the accumulation of differences between

https://doi.org/10.1017/S0001924000010721 Published online by Cambridge University Press

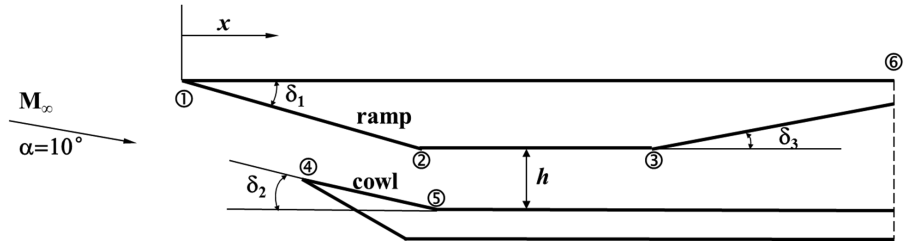


Figure 1. Geometric sketch of the supersonic inlet model.

the computational results and experimental data; i.e., positive and negative differences cannot offset each other. Third, if the differences between the computational results and experimental data are zero at all the measurement locations, the validation metric will be unity, indicating perfect agreement between the computational results and experimental data. Fourth, if the sum of the relative errors becomes large, the validation metric will approach zero[14,15].

A special feature of the scramjet inlet is that a large portion of the compression is achieved by an internal precombustion shock system. The engine component used for this internal compression is the isolator, which protects the inlet from upstream disturbances generated by the high-pressure combustion zone[16-17]. Herrmann[18] and Reinartz[19] studied the effect of varying the isolator length on the hypersonic inlet performance using experimental tests and numerical simulations. Chang[20-23] used the inlet studied in Refs 18,19 to validate the computational tool used for two-dimensional simulations of the internal compression flows of a hypersonic inlet.

However, to the extent of the knowledge of the authors, the effects of the different turbulence models and the different turbulence intensities and length scales specified in the inflow boundary condition for an internal compression supersonic inlet are rarely studied. The quantification of the level of agreement between computational results and experimental data, which is referred to as a validation metric, is also rarely found in available literature.

In the present study, the effects of various turbulence models and different turbulence intensities and length scales specified in the inflow boundary condition on the internal compression flows of a typical supersonic inlet were investigated. The level of agreement between the computational results and previously published experimental data were determined through both graphical and quantitative comparisons. Finally, the effect of different back-pressure ratios on the inlet flow field was also investigated.

2.0 PHYSICAL MODEL AND NUMERICAL METHOD

2.1 Physical model

To investigate the effects of different turbulence models, turbulence intensities and length scales on the internal compression flows of a supersonic inlet, the experimental model studied by Herrmann *et al*[18,19] was used to obtain data for evaluative comparison with the numerical method. This experiment is very valuable because it provides good spatial resolution of the wall pressure profiles and clear schlieren pictures of the supersonic flows through the internal compression inlet.

https://doi.org/10.1017/S0001924000010721 Published online by Cambridge University Press

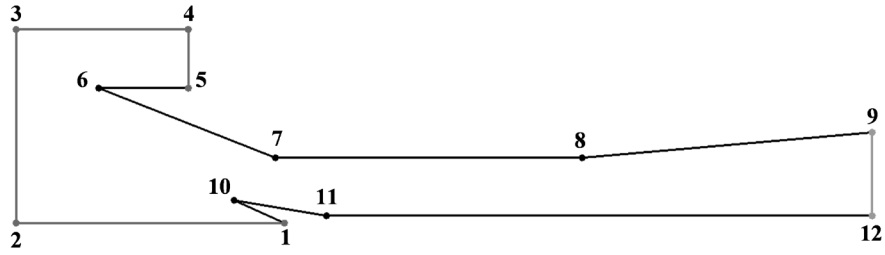


Figure 2. Numbers of the boundary points of the computational domain for the supersonic inlet model.

The overall inlet geometry is based on similar inlet models tested within the framework of earlier German studies[24,25]. In this original model geometry of the earlier German studies, two ramps deflect the flow before entering the inlet. However, due to the restrictions of the wind tunnel used in Refs 18 and 19, the experimental setup requires that the first outer compression ramp of the inlet geometry be omitted to attain the specified test conditions. Figure 1 is a geometric sketch of the supersonic inlet model. The major geometric parameters of the supersonic inlet are listed in Table 1; the unit of length is meters and the unit of angle is degrees. The design condition of the second ramp of the inlet used in Refs 24 and 25 is used as the freestream flow conditions at the inlet to the test section in Refs 18 and19, and listed in Table 2.

2.2 Numerical method

In the present study, the two-dimensional compressible Reynolds-averaged Navier–Stokes equations were solved using the density-based (coupled) implicit double precision FLUENT solver[2]. Four different turbulence models, namely, standard k-ε model[3], RNG k-ε model[4], realisable k-ε model[5], and SST k-ω model[12], were used to simulate the supersonic inlet flow to investigate their effect on the flow field.

The second-order spatially accurate upwind scheme that applies the advection upstream splitting method (AUSM) to the flux vector was utilised, the Green-Gauss cell-based gradient

Table 1
Geometric parameters of the supersonic inlet model

Quantity	Value
Isolator height h (m)	0·015
Location 1 (m)	0·0
Location 2 (m)	0·0457
Location 3 (m)	0·075
Location 4 (m)	0·035
Location 5 (m)	0·0589
Location 6 (m)	0·2
α (°)	10·0
δ_1 (°)	21·5
δ_2 (°)	9·5
δ_3 (°)	5·0

https://doi.org/10.1017/S0001924000010721 Published online by Cambridge University Press

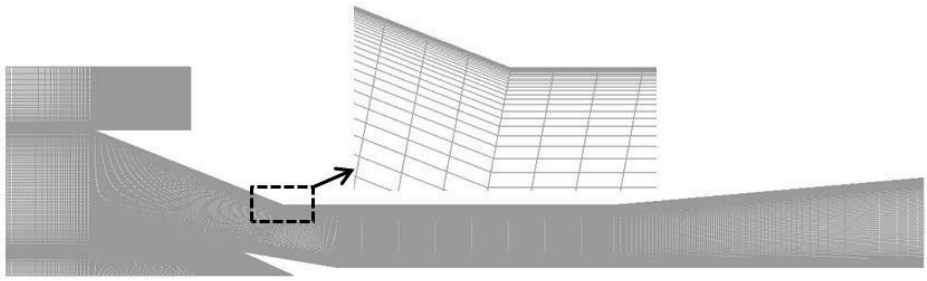


Figure 3. Computational domain and grid detail of the medium grid for the supersonic inlet model.

Table 2
Test conditions of the inlet model

M_∞	Re_∞ (1/m)	P_0 (kPa)	T_0 (K)
2·41	$5{\cdot}07 \times 10^7$	540	305

method was used to compute the gradients, and the Courant–Friedrichs–Levy number was maintained at 0·5 by using proper under-relaxation factors to ensure stability[26]. The standard wall functions based on the proposal of Launder and Spalding[27] were introduced into the flow in the near-wall region. In order to describe the locations of the boundary conditions, the boundary points of the computational domain are numbered and shown in Fig. 2, and the specified boundary conditions of the computational domain are listed in Table 3. As shown in Table 3, the boundary condition of the supersonic inflow (marked by line segments 1-2, 2-3, 3-4 shown in Fig. 2) was the pressure far-field that was equal to the test conditions of the inlet model listed in Table 2. The boundary condition employed in the line segment marked by 4-5 shown in Fig. 2 was also the pressure far-field. The boundary condition at the exit of the isolator (marked by line segment 9-12 shown in Fig. 2) was a specified back-pressure value. The adiabatic and no-slip boundary conditions were imposed along the walls (marked by line segments 5-6, 6-7, 7-8, 8-9, 1-10, 10-11, 11-12 shown in Fig. 2). The air was assumed to be a thermally and calorically perfect gas. The solutions were considered to converge if the residuals reached their minimum values after falling by more than four orders of magnitude, and the difference between the computed inflow and outflow mass fluxes fell below 0·5%. The residuals (L2-norm) for the RNG k-ε turbulence model are shown in Fig. 4.

At the same time, the computational domain was structured using the commercial software ICEM CFD, and three grid scales were used to analyse the grid independency in the numerical process, namely, coarse grid (497 × 66), medium grid (994 × 130), and refined grid (1,988 × 260). The grid scales considered here refer to the computational domain outlined by line 6-7, line 7-8, line 8-9, line 9-12, line 12-11, line 11-10, and line 10-6 in Fig. 2. To ensure accuracy in the solution of the turbulent flow, a value of y^+ less than 1 was used for the main portion of the wall flow region. The entire computational domain and grid detail of the medium grid are shown in Fig. 3.

https://doi.org/10.1017/S0001924000010721 Published online by Cambridge University Press

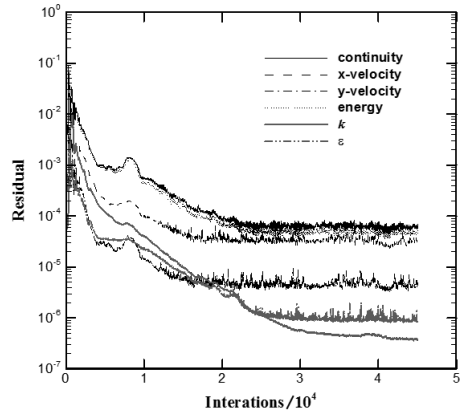


Figure 4. Residuals of the supersonic inlet computation using the RNG *k*-ε turbulence model.

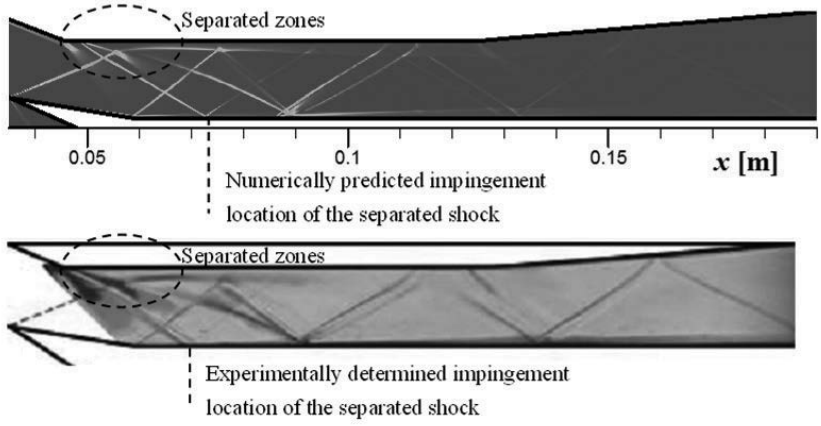


Figure 5. Comparison of the schlieren image (bottom) without throttling and the corresponding density gradient fields (top) for the computation using the RNG *k*-ε turbulence model.

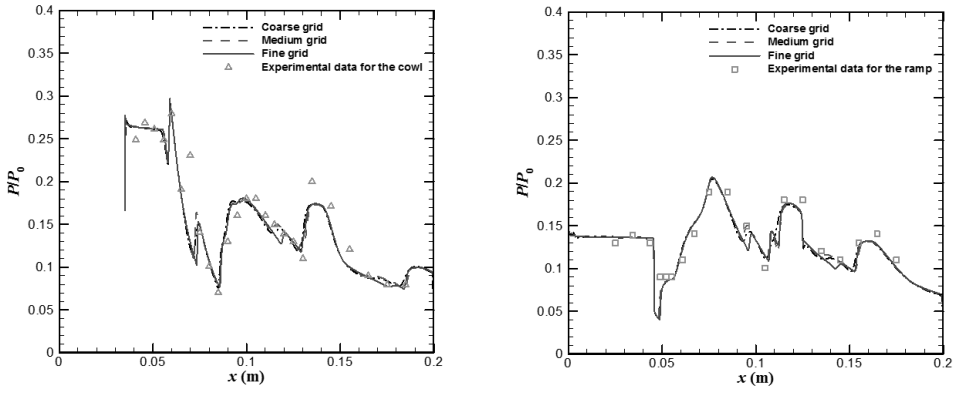
Table 3
Boundary conditions of the computational domain for the supersonic inlet model

Line segments	Boundary conditions
1-2, 2-3, 3-4, 4-5	Pressure far-field
5-6, 6-7, 7-8, 8-9, 1-10, 10-11, 11-12	No-slip
9-12	Pressure outlet

2.3 Accuracy analysis

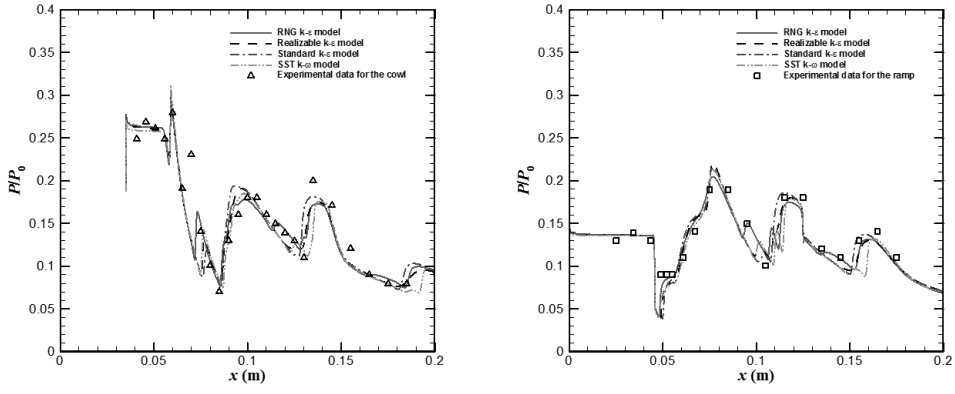
The accuracy of the present numerical investigation was evaluated by comparing it with the experimental data in Refs 18 and 19. Figure 5 is a comparison of the schlieren image without throttling and the corresponding density gradient fields obtained by computation using the RNG *k*-ε turbulence model, which reveals good overall agreement. The shock wave pattern, the separation, and the approximate boundary-layer thickness in the schlieren image are all present

https://doi.org/10.1017/S0001924000010721 Published online by Cambridge University Press



(a) cowl (b) ramp

Figure 6. Comparison of the wall pressure profiles for different grid scales using the RNG *k*-ε turbulence model.



(a) cowl (b) ramp

Figure 7. Comparison of the wall pressure profiles for different turbulence models without throttling.

Table 4
Validation metrics at the cowl and ramp locations for different grid scales

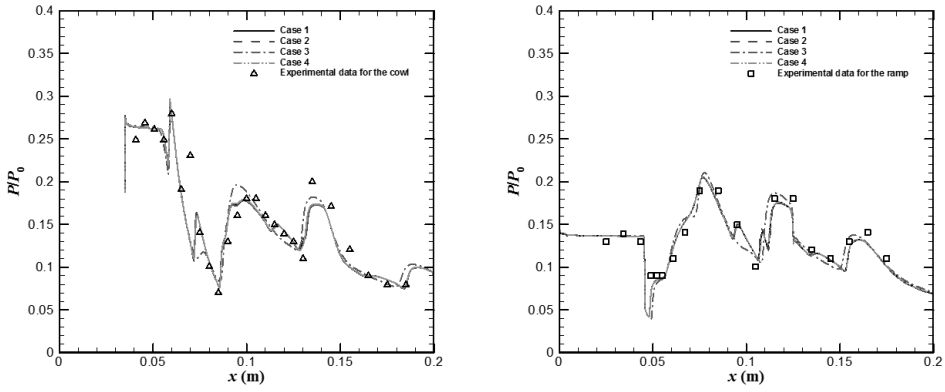
Item	Coarse grid	Medium grid	Refined grid
Cowl validation metric	0·908	0·920	0·919
Ramp validation metric	0·914	0·921	0·895

in the predicted results. The computed separation zone appears smaller than that obtained experimentally, which makes the separation shock weaker and causes it to impinge downstream of the measurement location on the cowl surface (see Fig. 5). The reason for the discrepancy is probably due to the shortcoming in the existing two-equation turbulence model with regard to its tendency to underpredict the flow separation[28]. Overall, the computational results for the supersonic inlet agree with physical aerodynamic concepts; this not only reveals the intersection between the oblique shock waves and the expansion waves but also reflects the primary internal flow characteristics of a typical supersonic inlet.

https://doi.org/10.1017/S0001924000010721 Published online by Cambridge University Press

Table 5
Validation metrics at the cowl and ramp for different turbulence models

Item	RNG *k*-ε	Realisable *k*-ε	Standard *k*-ε	SST *k*-ω
Cowl validation metric	0·920	0·900	0·872	0·902
Ramp validation metric	0·921	0·882	0·833	0·816



(a) cowl (b) ramp

Figure 8. Comparison of the wall pressure profiles for different turbulence intensities and turbulence length scales using the RNG *k*-ε model without throttling.

3.0 RESULTS AND DISCUSSION

In this section, the effects of the turbulence model and the freestream turbulence intensity and length scale specified in the inflow boundary condition are investigated through grid independency analysis. The effect of the back-pressure ratio on the properties of the flow field is also investigated.

3.1 Grid independency analysis

Figure 6 shows a comparison of the static pressure distributions along the cowl and on the ramp surfaces for three grid scales using the RNG *k*-ε turbulence model without throttling. The numerical results obtained for the three grid scales are in good agreement with the experimental data.

However, the use of only graphical comparison does not afford quantification of the numerical error owing to the different grid scales. The metric represented by Equation (1) is used to quantify the level of agreement between the computational results and experimental data. Table 4 lists the validation metrics for the cowl and ramp locations obtained from Equation (1) for the different grid scales. By definition, the validation metric has a value of 1 when there is perfect agreement[15]. In Table 4, the validation metric for the medium grid is the highest among those for the three grid scales. In other words, the level of agreement between the computational results and experimental data for the medium grid is the best according to the current validation metric.

At the same time, as can be seen in Table 4, the discrepancy between the validation metrics for the three grid scales is small. For the cowl, the variation percentage of the validation metric for the medium grid relative to the coarse grid is about 1·3%; for the refined grid relative to the coarse grid is about 1·2%. For the ramp, the variation percentage of the validation metric for the medium grid relative to the coarse grid is about 0·8%; for the refined grid relative to the coarse grid is about 2·1%. The grid scale makes only a slight difference and verifies the grid independency.

https://doi.org/10.1017/S0001924000010721 Published online by Cambridge University Press

The grid independency analysis confirmed that the grid resolution was sufficient. Thus, to reduce computational time, the medium grid was used for the following investigations.

3.2. Effect of the turbulence model

The computational results for the wall pressure profiles using four different turbulence models, namely, the RNG k-ε, realisable k-ε, standard k-ε, and SST k-ω models, were graphically compared with the experimental data (see Fig. 7). The results for all four turbulence models are in good overall agreement with the experimental data. However, the differences between the results obtained from the four turbulence models are not obvious if only using the graphical comparison.

To quantify the level of agreement between the computational results and experimental data, the metric represented by Equation (1) was used. Table 5 lists the validation metrics obtained from Equation (1) for the cowl and ramp locations when using the different turbulence models. The validation metrics for the cowl and ramp locations when using the RNG k-ε turbulence model are the highest, indicating that this model is more suitable for simulating the internal compression flow field through the supersonic inlet.

Overall, the quantitative and graphical comparisons reveal good agreement between the computational results and experimental data for the four turbulence models, with the agreement for the RNG k-ε model being the best. The numerical results for the RNG k-ε model can be used as a reference for investigating the effect of the turbulence intensity and turbulence length scale on the computation.

3.3 Effects of turbulence intensity and turbulence length scale

The turbulence intensity I is defined as the ratio of the root-mean-square of the velocity fluctuations u' to the mean flow velocity u_{avg}. The turbulence intensity at the core of a fully developed duct flow can be estimated using the following formula derived from an empirical correlation for pipe flows[2]:

$$I \equiv \frac{u'}{u_{avg}} = 0{\cdot}16\left(\mathrm{Re}_{D_H}\right)^{-1/8} \quad \ldots (2)$$

where D_H is the hydraulic diameter of the flow path, and Re_{DH} is the Reynolds number based on D_H.

The turbulence length scale l is a physical quantity related to the size of the energy-containing large eddies in turbulent flows. In fully developed duct flows, l is restricted by the size of the duct because the turbulent eddies cannot be larger than the duct. An approximate relationship between l and the size of the duct is as follows[2]:

$$l = 0{\cdot}07L \quad \ldots (3)$$

where L is the relevant dimension of the duct, and the factor of 0·07 is based on the maximum value of the mixing length in a fully developed turbulent pipe flow.

In the present study, four cases were used to investigate the effects of the different turbulence

Table 6
Specific turbulence intensity and turbulence length scale for the four cases

Item	Case 1	Case 2	Case 3	Case 4
Turbulence intensity, I (%)	2·7114	10·0	10·0	2·7114
Turbulence length scale, l (m)	0·00203	1·0	0·00203	1·0

https://doi.org/10.1017/S0001924000010721 Published online by Cambridge University Press

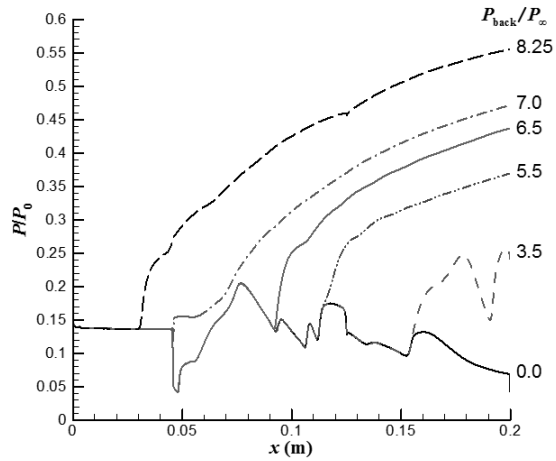


Figure 9. Ramp pressure distributions for different back-pressure ratios using the RNG *k*-ε model.

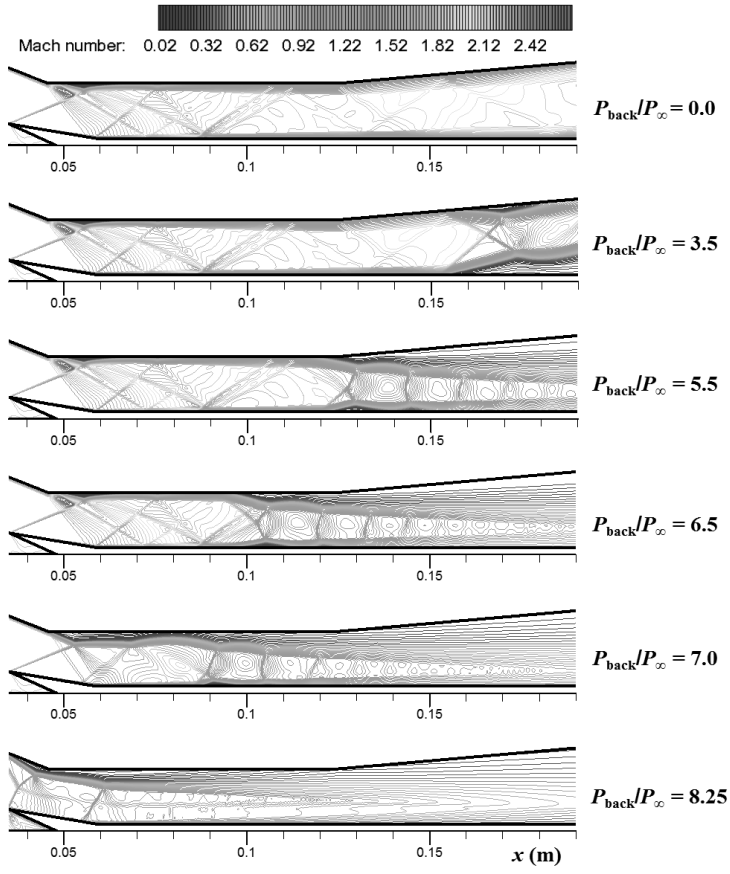


Figure 10. Mach number contour lines of the inlet internal flow fields for different back-pressure ratios using the RNG *k*-ε model.

https://doi.org/10.1017/S0001924000010721 Published online by Cambridge University Press

Table 7
Validation metrics for different turbulence intensities and length scales

Item	Case 1	Case 2	Case 3	Case 4
Cowl validation metric	0·922	0·920	0·889	0·923
Ramp validation metric	0·922	0·921	0·898	0·922

intensities and length scales specified in the boundary condition of the inflow for computation. The specific parameters are listed in Table 6.

The Reynolds number achieved on the supersonic test bed was $5{\cdot}07 \times 10^7$/m, and the height of the inlet was 0·029m. The Reynolds number at the inlet entrance was therefore $5{\cdot}07\times10^7 \times 0{\cdot}029 = 1{\cdot}47\times10^6$, which was substituted into Equation (2) to calculate the value of I for Case 1. The height of the inlet was substituted into Equation (3) to calculate the value of l for Case 1.

The default values[2] of I and l in the FLUENT solver were used for Case 2. The value of I for Case 2 and the value of l for Case 1 were used for Case 3. The value of I for Case 1 and the value of l for Case 2 were used for Case 4.

Figure 8 shows a comparison of the wall pressure profiles for the different turbulence intensities and length scales using the RNG k-ε model without throttling. Only the predicted results for Case 3 and the experimental data are obviously different from each other. However, although the turbulence intensity and length scale for the four cases are quite different, all the results are in good overall agreement with the experimental data. In other words, there are no remarkable differences between the wall pressure profiles obtained from the different turbulence parameters, and this is consistent with the observations obtained by Erdem and Kontis[29].

To quantify the level of agreement between the computational results and experimental data, the metric represented by Equation (1) was used. Table 7 lists the validation metrics obtained in Equation (1) for the cowl and ramp locations corresponding to the four cases. It is obvious that the validation metric for Case 3 is the lowest, whereas those for the other three cases are basically the same. This observation is similar to that in Fig. 8.

Overall, the quantitative and graphical comparisons show that it is better to use the default values of parameters I and l in the FLUENT solver, or the empirical formula expressed by Equations (2) and (3), to calculate the values of I and l when specifying the turbulence quantities for the boundary condition of the inflow. This approach produces the best agreement between the numerical results and experimental data. When referring to case 2 and case 4 as shown in Table 7, the results obtained using the default value of l in the FLUENT solver and the variable magnitudes of turbulence intensity I are only slightly different from each other. However, when referring to case 3 as shown in Table 7, using the default value of I in the FLUENT solver and the value of l calculated with the empirical formula (Equation (3)) decreases the accuracy of the predictions compared to the other three cases.

3.4 Effect of back-pressure ratio

To investigate the effect of the back-pressure ratio on the properties of the flow field of the internal compression supersonic inlet, six back-pressure ratios ranging from 0 to 8·25 were used. The back-pressure ratio (P_{back}/P_∞) is defined as the ratio of the back-pressure to the freestream static pressure.

The ramp surface pressure distributions computed using the RNG k-ε model for different back-pressure ratios are shown in Fig. 9, and the corresponding Mach number contours are shown in Fig. 10.

https://doi.org/10.1017/S0001924000010721 Published online by Cambridge University Press

When $P_{back}/P_{\infty} = 0$, i.e., the specified back-pressure value at the exit of the isolator is zero. The flow expands around the corner of the compression ramp edge. Slightly downstream, the impingement of the cowl lip shock on the ramp induces a small separation in the boundary layer, and the resultant separation and reattachment shocks are visible as two lines divided by the red coloured expansion. Another primary shock wave, which is induced by the cowl deflection angle, crosses the separation and reattachment shocks; it is reflected at the ramp before it impinges at almost the same location as the reattachment shock on the cowl surface. The repeatedly reflected shocks downstream are visibly weakened.

When $P_{back}/P_{\infty} = 3{\cdot}5$, the main flow remains supersonic until it is downstream of the diffusing section. Consequently, the complex pattern of the interaction between the shock wave and the expansion wave in the isolator remains the same as that without the back-pressure. Downstream of the diffusing section, the back-pressure separates the upper and lower boundary layers, and a shock wave pattern is generated by two intersecting oblique shock waves. In this case, there is no shock train.

When $P_{back}/P_{\infty} = 5{\cdot}5$, an incipient shock train is detectable in the diffuser. The two intersecting oblique shock waves induced by the separation remain as described in the case of $P_{back}/P_{\infty} = 3{\cdot}5$. Because of the constriction of the main flow, especially on the ramp side, the flow accelerates again and enters the subsonic regime with a normal shock. The flow thereafter repeats the acceleration and deceleration until it becomes more homogeneous. The actual shock train begins at an approximate axial position of $x = 0{\cdot}13$m. Upstream of this position, there is a compression/expansion interaction pattern, as indicated by the corresponding pressure distribution in Fig. 9, which is typical of reflected oblique shock waves, although there is no continuous pressure buildup. At $x = 0{\cdot}13$ m, an initial normal shock is immediately followed by two intersecting oblique shock waves; the onset of the shock train can be clearly observed in the figure. The primary shock is followed by two secondary normal shock waves in the main flow, which is increasingly constricted by the growing boundary layers.

When $P_{back}/P_{\infty} = 6{\cdot}5$, the flow pattern remains as described in the case of $P_{back}/P_{\infty} = 5{\cdot}5$. However, the shock train moves upstream into the isolator. When $P_{back}/P_{\infty} = 7{\cdot}0$, the entire ramp boundary-layer separates up to the expansion region; when $P_{back}/P_{\infty} = 8{\cdot}25$, a fully developed normal shock train appears in the flow field. When the back-pressure ratio is sufficiently high, the shock train is pushed out of the supersonic inlet, and the unstart phenomenon occurs.

4.0 CONCLUSIONS

In this study, the effects of different turbulence models and the different turbulence intensities and turbulence length scales specified in the inflow boundary condition for the numerical simulation of an internal compression supersonic inlet were investigated, and the level of agreement between the computational results and available experimental data were validated by both graphical and quantitative comparisons. Finally, the effect of the back-pressure ratio on the properties of the flow field was investigated. The conclusions are as follows:

- The validation metric employed in the present study is suitable for evaluating the discrepancy between the predicted results and experimental data, and the validation process is effective and efficient.
- The RNG k-ε turbulence model is more suitable for simulating the internal compression flow field in the supersonic inlet compared to the realisable k-ε, standard k-ε, and SST k-ω models.
- The agreement between the predicted results and experimental data is best when the either default values of parameters I and l in the FLUENT solver, or the empirical formula expressed by Equations (2) and (3) is used to calculate the values of I and l.

https://doi.org/10.1017/S0001924000010721 Published online by Cambridge University Press

- The shock train pattern varies between the oblique mode and the fully developed normal mode with increasing back-pressure ratio, and the unstart phenomenon occurs when the back-pressure ratio is sufficiently high.

ACKNOWLEDGEMENTS

The authors would like to express their gratitude for the financial support provided by the Fund of Innovation, Graduate School of NUDT (No.B140105), the Hunan Provincial Natural Science Foundation of China (No.12jj4047), and the Science Foundation of National University of Defense Technology (No.JC14-01-01). The authors are also grateful to the reviewers for their extremely constructive comments.

REFERENCE

1. WILCOX, D.C. Progress in hypersonic turbulence modeling, AIAA paper 91-1785, 1991.
2. Fluent Inc, ANSYS, Inc, ANSYS FLUENT 13.0 Theory Guide, 2010.
3. LAUNDER, B.E. and SPALDING, D.B. *Lectures in Mathematical Models of Turbulence*, Academic Press, London, England, 1972.
4. CHOUDHURY, D. Introduction to the Renormalisation Group Method and Turbulence Modeling, Fluent Inc, Technical Memorandum TM-107, 1993.
5. SHIH, T.H., LIOU, W.W., SHABBIR, A., YANG, Z. and ZHU, J. A new k-ε eddy-viscosity model for high Reynolds number turbulent flows, *Computers & Fluids*, 1995, **24**, (3), pp 227-238.
6. CHRISTOPHER, L.R. Compressibility considerations for k-ω turbulence models in hypersonic boundary-layer applications, *J Spacecraft and Rockets*, 2010, **47**, (1), pp 11-20.
7 WILCOX, D.C. Reassessment of the scale determining equation for advanced turbulence models, *AIAA J*, 1988, **26**, (11), pp 1299-1310.
8. WILCOX, D.C. Multiscale model for turbulent flows, *AIAA J*, 1988, **26**, (11), pp 1311-1320.
9. WILCOX, D.C. Turbulence Modeling For CFD, DCW Industries, Inc., La Canada, California, USA, 1998.
10. MENTER, F.R. Two-equation eddy-viscosity turbulence models for engineering applications, *AIAA J*, 1994, **32**, pp 1598-1605.
11. MENTER, F.R., KUNTZ, M. and LANGTRY, R. Ten years of industrial experience with the SST turbulence model, *Turbulence*, *Heat and Mass Transfer,* 2003, **4**, pp 625-632.
12. MENTER, F.R. Review of the SST turbulence model experience from an industrial perspective, *Int J Computational Fluid Dynamics*, 2009, **23**, (4), pp 305-316.
13. KAPOOR, K., ANDERSON, B.H. and SHAW, R.J. Comparative study of turbulence models in predicting hypersonic inlet flows, NASA Technical Memorandum 105720, AIAA Paper 92-3098, 1992.
14. OBERKAMPF, W.L. and TRUCANO, T.G. Validation methodology in computational fluid dynamics, AIAA Paper 2000-2549, 2000.
15. OBERKAMPF, W.L. Verification and validation in computational fluid dynamics, *Progress in Aerospace Sciences*, 2002, **38**, pp 209-272.
16. VAN WIE, D.M. Scramjet Inlets, Scramjet Propulsion, CURRAN, E.T. and MURTHY, S.N.B.(Eds), **189**, *Progress in Astronautics and Aeronautics*, 2000, AIAA, Reston, VA, USA, pp 447-511.
17. HUANG, W., WANG, Z.G., POURKASHANIAN, M., MA, L. INGHAM, D.B., LUO, S.B., LEI, J. and LIU, J. Numerical invesitgation on the shock wave transition in a three-dimensional scramjet isolator, *Acta Astronautica,* 2011*,* **68**, pp 1669-1675.
18. HERRMANN, C.D. and KOSCHEL, W.W. Experimental investigation of the internal compression of a hypersonic intake, AIAA Paper 2002-4130, 2002.
19. REINARTZ, B.U., HERRMANN, C.D. and BALLMANN, J. Aerodynamic performance analysis of a hypersonic inlet isolator using computation and experiment, *J Propulsion and Power*, 2003, **19**, (5), pp 868-875.
20. CHANG, J., YU, D., BAO, W., XIE, Z. and FAN, Y. A CFD assessment of classifications for hypersonic inlet start/unstart phenomena, *Aeronaut J*, 2008, **113**, (1142), pp 263-271.
21. CHANG, J., YU, D., BAO, W. and FAN, Y. Operation pattern classification of hypersonic inlets, *Acta Astronautica*, 2009, **65**, pp 457-466.

https://doi.org/10.1017/S0001924000010721 Published online by Cambridge University Press

22. CHANG, J. BAO, W., YU, D., FAN, Y., and SHEN, Y. Effects of wall cooling on performance parameters of hypersonic inlets, *Acta Astronautica*, 2009, **65**, pp 467-476.
23. CHANG, J., FAN, Y., BAO, W., YU, D. and SHEN, Y. Unstart margin control of hypersonic inlets, *Acta Astronautica*, 2010, **66**, pp 78-87.
24. SCHMITZ, M.C. and BISSINGER, N.C. Design and testing of a 2D fixed geometry hypersonic intake, AIAA Paper 98-1529, 1998.
25. WALTHER, R., KOSCHEL, W., SABELNIKOV, V., KORONTSVIT, Y. and IVANOV, V. Investigations into the aerothermodynamic characteristics of scramjet components, International Society for Air Breathing Engines, ISABE Paper 97-7085, 1997.
26. HUANG, W., WANG, Z.G., INGHAM, D.B., MA, L. and POURKASHANIAN, M. Design exploration for a single expansion ramp nozzle (SERN) using data mining, *Acta Astronautica*, 2013, **83**, pp 10-17.
27. LAUNDER, B.E. and SPALDING, D.B. The Numerical computation of turbulent flows, *Computer Methods in Applied Mechanics and Engineering*, 1974, **3**, pp 269-289.
28. HUANG, P.G. and COAKLEY, T.J. Turbulence modeling for complex hypersonic flows, AIAA Paper 93-0200, 1993.
29. ERDEM, E. and KONTIS, K. Numerical and experimental investigation of transverse injection flows, *Shock Waves*, 2010, **20**, pp 103-118.

https://doi.org/10.1017/S0001924000010721 Published online by Cambridge University Press